



Non-field-aligned Proton Beams and Their Roles in the Growth of Fast Magnetosonic/Whistler Waves: Solar Orbiter Observations

Xingyu Zhu¹ , Jiansen He¹ , Die Duan¹ , Daniel Verscharen² , Christopher J. Owen² , Andrey Fedorov³ , Philippe Louarn³, and Timothy S. Horbury⁴

¹ School of Earth and Space Sciences, Peking University No.5 Yiheyuan Road, Haidian District Beijing 100871, People's Republic of China; jshept@pku.edu.cn

² Mullard Space Science Laboratory, University College London, Dorking RH5 6NT, UK

³ Institut de Recherche en Astrophysique et Planétologie, 9, Avenue du Colonel ROCHE, BP 4346, F-31028 Toulouse Cedex 4, France

⁴ Space and Atmospheric Physics, The Blackett Laboratory, Imperial College London, London SW72AZ, UK

Received 2023 March 11; revised 2023 May 4; accepted 2023 May 13; published 2023 August 14

Abstract

The proton beam is an important population of the non-Maxwellian proton velocity distribution in the solar wind, but its role in wave activity remains unclear. In particular, the velocity vector of the proton beam and its influence on wave growth/damping have not been addressed before. Here we explore the origin and the associated particle dynamics of a kinetic wave event in the solar wind by analyzing measurements from Solar Orbiter and comparing them with theoretical predictions from linear Vlasov theory. We identify the waves as outward-propagating circularly polarized fast magnetosonic/whistler (FM/W) waves. The proton's velocity distribution functions can destabilize FM/W waves. According to linear Vlasov theory, the velocity fluctuations of the core and the beam associated with FM/W waves render the original field-aligned background drift velocity non-field-aligned. This non-field-aligned drift velocity carrying the information of the velocity fluctuations of the core and the beam is responsible for the wave growth/damping. Specifically, for the FM/W waves we analyze, the non-field-aligned fluctuating velocity of the beam population is responsible for the growth of these unstable waves in the presence of a proton beam. In contrast, the core population plays the opposite role, partially suppressing the wave growth. Remarkably, the observed drift velocity vector between the core and the beam is not field aligned during an entire wave period. This result contrasts the traditional expectation that the proton beam is field aligned.

Unified Astronomy Thesaurus concepts: [Solar wind \(1534\)](#); [Heliosphere \(711\)](#)

Supporting material: [animation](#)

1. Introduction

In the solar wind at heliocentric distances (R) within 1 au, a typical feature of the proton (p) velocity distribution function (VDF) is that it comprises two populations: a primary core (c) and a drifting beam (b) (Marsch 1991, 2006; Verniero et al. 2020). Observations in high-speed streams near 0.3 au (Marsch et al. 1982b) show that the core is usually anisotropic with $T_{\perp,c}/T_{\parallel,c} > 1$, where $T_{\perp,c}$ and $T_{\parallel,c}$ are the core's perpendicular and parallel kinetic temperatures, respectively. Observations at 1 au (Hellinger et al. 2006; Maruca et al. 2011; Servidio et al. 2014) indicate that both $T_{\perp,c}/T_{\parallel,c} > 1$ and $T_{\perp,c}/T_{\parallel,c} < 1$ are often observed. The drift speed, determined by the velocity difference between the two peaks in the proton VDF, has a positive correlation with the solar wind speed (Marsch et al. 1982b). Tu et al. (2004) statistically analyze over 600 proton VDFs and find that the normalized drift speed has a positive correlation with the core's parallel plasma beta (β). In their work, they determine a critical speed of the 1D reduced VDF, at which the VDF has a minimum between two peaks, to separate the core and beam. Then, they calculate the first-order moment of each part of the 1D VDF to obtain the velocities of the core and beam. β is defined as the ratio of the thermal energy of the plasma to the magnetic field energy.

A drifting bi-Maxwellian distribution can parameterize an observed proton VDF when it shows a distinguishable secondary population. Occasionally, the observed proton VDF deviates from a drifting bi-Maxwellian distribution exhibiting non-Maxwellian (e.g., nongyrotropic) features (Astudillo et al. 1996; He et al. 2015). For the determination of the plasma parameters (e.g., number density, flow velocity, and temperature) of the core and beam populations of protons for further analysis, the two-component bi-Maxwellian fitting is regarded as a feasible and reasonable method. Based on Helios observations, a body of work (Marsch et al. 1982b; Matteini et al. 2007; Hellinger et al. 2011, 2013; Āurovcova et al. 2019) illustrates that the protons undergo perpendicular heating and parallel cooling or heating from 0.3 to 1 au. Both the proton core thermal anisotropy ($T_{\perp,c}/T_{\parallel,c}$) and the proton beam drift speed statistically increase with the flow speed of the solar wind (Marsch et al. 1982b). Using measurements from Parker Solar Probe (PSP) at 0.17 au $< R < 0.5$ au, Huang et al. (2020) find that the radial evolution of $T_{\perp,p}$ and $T_{\parallel,p}$ in the fast solar wind follows $T_{\perp,p} \sim R^{-0.48}$ and $T_{\parallel,p} \sim R^{-0.98}$, respectively. This result shows a stronger perpendicular heating and parallel cooling compared to the Helios observations at 0.3 au $< R < 1$ au, which reveal power indexes of -0.83 and -0.54 , respectively (Hellinger et al. 2011). According to Huang et al. (2020), the perpendicular heating and parallel cooling are more significant within 0.3 au. The proton parallel temperature is more prominent inside the magnetic reversals/kinks than the ambient background solar wind (Woolley et al. 2020; Woodham et al. 2021), which means that some heating

mechanisms may play a critical role within the magnetic kink region, leading to less cooling.

Despite disputes for decades, we still do not definitely understand the mechanisms concerning the solar wind acceleration, the formation of the nonadiabatic temperature profile, and the tendency to preferentially heat heavier ions (Freeman 1988; Tu & Marsch 1997; Isenberg & Vasquez 2007; Cranmer et al. 2009; Kasper et al. 2017; Zhao et al. 2020b; Wu et al. 2020). On account of the scarce binary Coulomb collisions of the solar wind plasma, wave–particle interactions dominantly regulate and shape the spatiotemporal evolution of the VDF. Cyclotron resonance is believed to play an essential role in governing the observed heating behavior (Marsch et al. 1982a; Cranmer 2001; Tu & Marsch 2002; Kasper et al. 2013; He et al. 2015; Zhao et al. 2020a; Jeong et al. 2020; Bowen et al. 2022).

The departure from local thermodynamic equilibrium provides sufficient free energy to drive kinetic instabilities generating unstable waves (Chen et al. 2016; Gary et al. 2016; Klein et al. 2021). The instabilities have been comprehensively discussed in the framework of linear theory, considering both temperature anisotropies for the two proton populations and the differential flow along the background magnetic field (Gary 1993; Yoon 2017). According to the theory of space plasma microinstabilities (Gary 1993), both Alfvén/ion-cyclotron (A/IC) and fast magnetosonic/whistler (FM/W) waves may grow unstable in specific parametric regimes through resonant or non-resonant wave–particle interactions.

In observations, cyclotron waves are frequently present in the solar wind. Statistical works (Jian et al. 2009; He et al. 2011; Jian et al. 2014; Boardsen et al. 2015; Zhao et al. 2019; Bowen et al. 2020a; Klein et al. 2021) have shown that the quasi-parallel (anti-parallel) propagating cyclotron waves within 1 au, lasting from seconds to several hours, have high degrees of circular polarization. Notably, Boardsen et al. (2015) show that the radial scaling of the wave power of left-handed waves beyond 0.3 au is consistent with source regions closer to the Sun. In contrast, cyclotron wave storms within 0.3 au are speculated to be locally generated based on the findings of their lack of radial scaling (Bowen et al. 2020b). PSP studies show the presence of ion-scale waves, as well as significant evidence that the associated proton VDFs are prone to kinetic instability, suggesting the local growth of these waves (Verniero et al. 2020; Klein et al. 2021; Verniero et al. 2022). A kinetic wave event in the inner heliosphere solar wind shows a clear dispersion relationship of the outward-propagating FM/W wave and a growth rate spectrum reflecting the rapid growing process of the wave event (He et al. 2022). We note that Bowen et al. (2020a) investigate the properties of magnetic and electric field fluctuations associated with coherent ion-scale waves. A comprehensive study of wave properties and wave–particle interactions needs to incorporate the properties of particle species/populations associated with the wave fluctuations. However, the wave-associated polarization properties of the core and the beam and their different roles in the wave evolution remain unclear, which is essential for our understanding of the underlying physics of the wave–particle interactions.

Previous observational work mainly focuses on the properties of the parallel drift velocity between the proton core and beam populations (Marsch et al. 1982b; Matteini et al. 2007; Hellinger et al. 2011; Āurovcova et al. 2019). The proton beam

is usually regarded as responsible for the wave instability associated with ion kinetics (Chen et al. 2016; Bowen et al. 2020b; Verniero et al. 2020; Klein et al. 2021). However, the bulk motions of the core and the beam can be different in the perpendicular direction during one period of the wave. This effect results in a fluctuating differential flow in the perpendicular direction, which has not been addressed before. Moreover, distinct roles of each proton population in the wave growth/damping have not been investigated based on observations.

In this work, we investigate the propagation and polarization properties of a cyclotron wave event by comparing the observations with predictions from linear Vlasov theory. In addition, we analyze and explore the full 3D kinetic features of the core and the beam, along with their distinct roles for the wave, using linear Vlasov theory. Finally, we statistically study the non-field-aligned beam features using the measured VDF during the time interval of the cyclotron wave event.

2. Observational Analysis and Model Comparison

2.1. Investigation of a Cyclotron Wave Event

We use the magnetic field data from the MAG instrument (Horbury et al. 2020) on board the Solar Orbiter (SolO) spacecraft, with a cadence of 16 vectors s^{-1} . We use the ion VDF data from Proton-Alpha Sensor (PAS), which is part of the Solar Wind Analyzer (SWA) suite (Owen et al. 2020). PAS measures a complete ion VDF in a matrix of (96, 9, 11) elements (energy, elevation, azimuth), with a 5° angular resolution (Lavraud et al. 2021; Louarn et al. 2021; Matteini et al. 2021). PAS has two major sampling modes. The normal mode has a sampling rate of 4 s, and the time duration to perform the full energy and elevation sweeping is 1 s. For every 300 s, PAS raises the sampling rate and operates in “snapshot mode” for a duration of 8 s with a sampling cadence of 0.25 s.

Figure 1 shows an overview of the wave event lasting about 30 minutes from 11:30:00 to 12:00:00 on 2020 August 2. During this interval, SolO is located at a heliocentric distance of $R \sim 0.75$ au, a latitude of $-1^\circ 6'$, and a longitude of 200° in the HelioGraphic Inertial (HGI) coordinates. The average ion density, ion temperature, and ion bulk velocity are 6.2 cm^{-3} , 12.4 eV , and 372.4 km s^{-1} , respectively. B_R is around -6 nT (Figure 1(a)), indicating that SolO is in the inward magnetic sector. The ion gyrofrequency is 0.09 Hz . The frequencies in the spacecraft frame corresponding to the ion inertial length ($f_{d_i} = V_{sw}/2\pi d_i$) and thermal gyroradius ($f_{\rho_i} = V_{sw}/2\pi \rho_i$) under Taylor’s frozen-in hypothesis are 0.65 and 0.99 Hz , respectively, where d_i represents the ion inertial length, ρ_i represents the ion thermal gyroradius, and V_{sw} denotes the solar wind speed. Significant wave-like fluctuations ($\delta B/B_0 \sim 0.1$) are visible in the time series of B_T and B_N .

To obtain the fluctuation properties, we first apply a wavelet transform (Farge 1992) to the magnetic field time series in the frequency range between 0.01 and 1 Hz. With these wavelet coefficients, we then diagnose the propagation and polarization properties using the singular value decomposition (SVD) method (Santolik et al. 2003). In the range $0.1 \text{ Hz} < f < 0.5 \text{ Hz}$, we identify the polarization as right-handed about $\mathbf{B}_{0,\text{local}}$ (sense of polarization $\sim +1$) (Figure 1(c)), and the fluctuations are nearly circularly polarized (ellipticity ~ 1) (Figure 1(d)). $\theta_{k,B_0} < 10^\circ$ (Figure 1(e)) and $\theta_{dB,B_0} \sim 90^\circ$ (Figure 1(f)). The meanings of the above symbols are as follows. $\mathbf{B}_{0,\text{local}}$ denotes the local mean

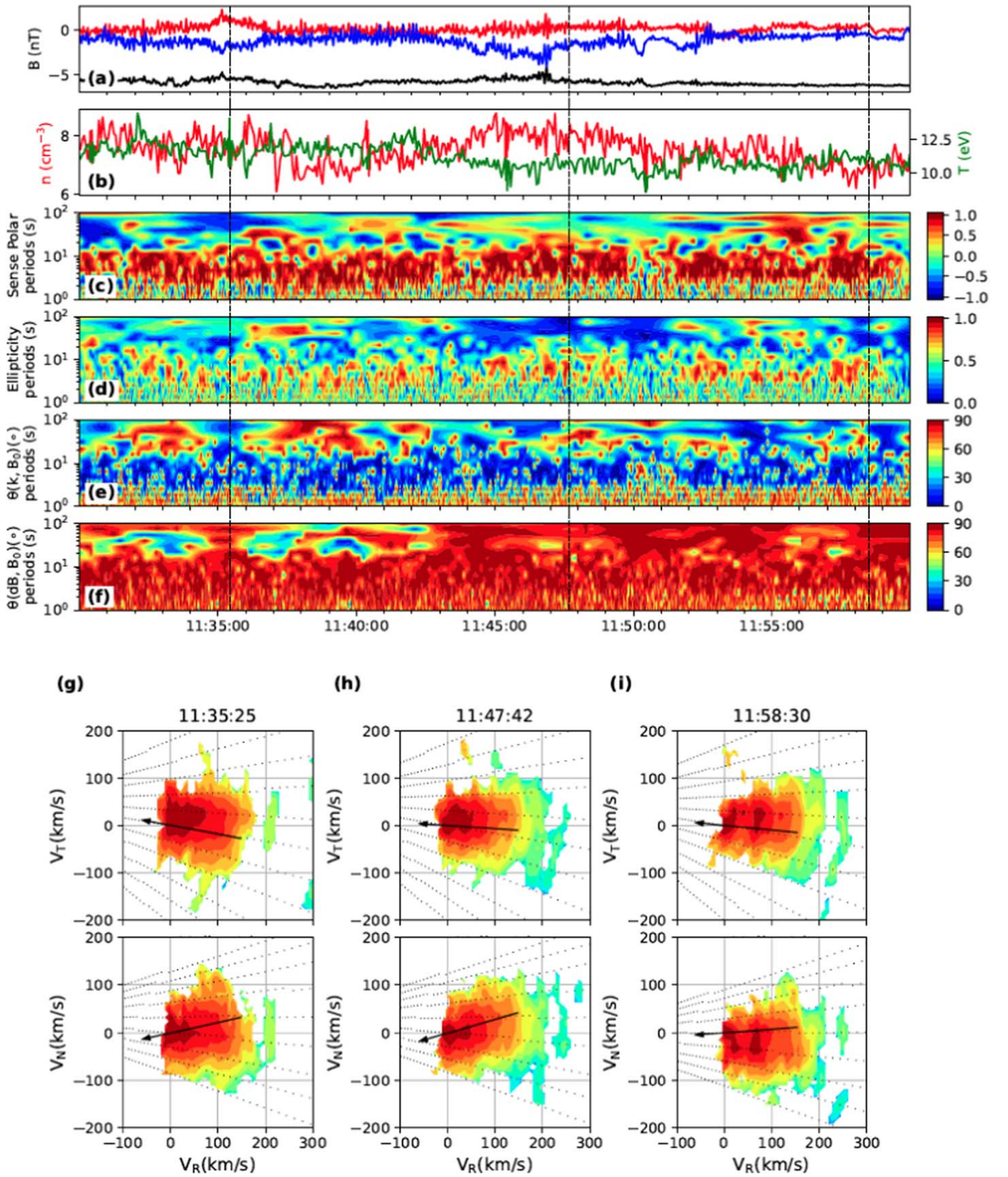


Figure 1. A cyclotron wave event as measured by SoLO on 2020 August 2. (a) Time series of the magnetic field components (B_R , B_T , and B_N) in RTN coordinates. (b) Time series of the proton number density, n , and the proton kinetic temperature, T . (c) Sense of polarization with respect to $\mathbf{B}_{0, \text{local}}$, where +1 and -1 represent the right-hand and left-hand polarization, respectively. (d) Ellipticity. (e) θ_{k, B_0} . (f) θ_{dB, B_0} . (g–i) Slices of the measured VDFs in the $V_T - V_R$ and $V_N - V_R$ planes at three times. The back arrow points to the instant magnetic field direction. The dots in each panel denote the positions of energy bins of PAS.

background magnetic field. Ellipticity is represented by the ratio of the middle and the maximum eigenvalues, $\lambda_{\text{mid}}/\lambda_{\text{max}}$. θ_{k, B_0} is the angle of the wavevector \mathbf{k} with respect to $\mathbf{B}_{0, \text{local}}$, where the direction of \mathbf{k} is represented by the direction of the eigenvector corresponding to the minimum eigenvalue, λ_{min} . θ_{dB, B_0} is the angle between the magnetic field fluctuation, $d\mathbf{B}$, and $\mathbf{B}_{0, \text{local}}$, where the direction of the eigenvector corresponding to λ_{max} stands for the direction of $d\mathbf{B}$. At this stage, we can only conclude that the wave-like fluctuations are related to quasi-parallel circularly polarized ion-scale waves, either outward-propagating FM/W waves or inward-propagating A/IC waves. In the next subsection, we analyze the kinetic instability of the observed proton VDF using linear Vlasov theory. We find that an outward-propagating FM/W mode stands out from the possible wave candidates owing to its largest growth rate. Hence, we infer that the observed fluctuations are most likely FM/W waves. Such a combination of observational and theoretical analysis has been commonly used in the literature for analyzing the intrinsic nature of waves (Klein et al. 2014; Wicks et al. 2016; Woodham et al. 2019; Bowen et al. 2020a). To unambiguously determine the wave nature, we would require additional observational data (e.g., electric field) in the same frequency band in addition to the magnetic field data. Representative VDFs in the frame of the proton core velocity at three times are displayed in Figures 1(g)–(i). For each measured proton VDF, we first transform the velocity of each energy bin in the instrument coordinates to RTN coordinates. Then, we move the frame center to the velocity of the maximum of the VDF. We establish a regular mesh grid in this coordinate system. We set the ranges for V_R , V_T , and V_N to $[-100, 300]$ km s $^{-1}$, $[-200, +200]$ km s $^{-1}$, and $[-200, +200]$ km s $^{-1}$, respectively. We interpolate the velocity of each bin to this regular mesh grid and obtain the contour of the proton VDF. All these VDFs exhibit a faster beam in the direction away from the Sun. In addition, during this wave activity interval, most VDFs show that the beam’s drift velocity is not exactly field aligned as illustrated in the representative VDFs.

2.2. Instability Analysis, Wave Polarization Properties, and Non-field-aligned Beam Feature

The appropriate coverage of the relevant 3D kinetic features of the core and the beam is crucial to disentangle the wave–particle interaction physics and the evolution of the distribution function. To address this issue, we apply the “genetic algorithm” (GA) technique (Holland 1992) to directly fit the measured 3D VDF in field-aligned coordinates using a two-component bi-Maxwellian distribution function:

$$f(v_{\parallel}, v_{\perp 1}, v_{\perp 2}) = \sum_{j=c,b} \frac{n_j}{v_{\text{th},j}^2 v_{\text{th},j} v_{\text{th},j} \sqrt{\pi}^3} \exp \left(-\frac{(v_{\parallel} - U_{\parallel,j})^2}{v_{\text{th},j}^2} - \frac{(v_{\perp 1} - U_{\perp 1,j})^2}{v_{\text{th},j}^2} - \frac{(v_{\perp 2} - U_{\perp 2,j})^2}{v_{\text{th},j}^2} \right). \quad (1)$$

GA is a powerful technique to optimize the parameters relying on biologically inspired operators, such as selection, mutation, and crossover (Holland 1992). It enables the global optimum by optimizing a fitness function, in contrast to the traditional Levenberg–Marquardt (LM) method, which is more likely to attain the local optimum. Previous works (Gary et al. 2016; Wicks et al. 2016; Bowen et al. 2020b) on fitting observed VDFs usually assume that the beam only drifts along the local magnetic field. They employ the fitting procedure in 1D or 2D

velocity space, which requires fewer fitting parameters. Since we need the knowledge of the 3D parameters of the core and beam populations, we have 12 parameters to fit, including the perpendicular velocities of the core and beam. In practice, we find that, compared with the LM method, GA is a more efficient technique for fitting the 3D VDF, returning more fitting parameters. The fitness function we choose is

$$\text{fitness} = \sum_{i=0}^N \sqrt{\frac{(f_{i,\text{obs}} - f)^2}{N}}, \quad (2)$$

where i is the index of N measured VDF points in velocity space and $f_{i,\text{obs}}$ is the i th measured VDF value. The GA technique finds the optimal fit parameters by minimizing the absolute value of the fitness function.

We thereby simultaneously obtain 12 fit parameters: the number densities (n_j), the bulk velocity components in the three directions ($U_{\parallel,j}$, $U_{\perp 1,j}$, and $U_{\perp 2,j}$), and the thermal velocities ($v_{\text{th},j}$ and $v_{\text{th},j}$) for the core and the beam. Figures 2(a) and (b) show an example of the fitting results for the VDF measured at 11:30:18. The physical parameters at this time are the following: $n_b/n_c \sim 0.48$, $T_{\perp,c}/T_{\parallel,c} \sim 1.72$, $T_{\perp,b}/T_{\parallel,b} \sim 0.92$, $V_{d\parallel}/V_A = (U_{\parallel,b} - U_{\parallel,c})/V_A \sim 1.72$, where $V_A = |\mathbf{B}_0|/\sqrt{\mu_0 m_p (n_c + n_b)}$ is the local Alfvén speed and $V_{d\parallel}$ is the drift velocity along the magnetic field direction.

Our fit algorithm considers all measured points in 3D velocity space and aims to yield an optimal fit to the full 3D VDF. In practice, the value of the fitness function converges after about 100 generations. This means that the fitness function reaches its global minimum value. We choose the fitting results at the 300th generation to guarantee the convergence of the results. A two-component bi-Maxwellian distribution can never perfectly model a measured 3D VDF. There are some factors that potentially influence the quality of the 3D fitting results. For example, the proton beam is not necessarily an ideal drifting bi-Maxwellian distribution, the proton core is agyrotropic, there is a statistical uncertainty in measurement, and our measurements suffer from the finite sweeping time when collecting particles.

We study the stability of the VDF at 11:30:18 in the proton core rest frame based on the linear Vlasov theory (Stix 1992). The degree of stability is independent of the reference frame we choose. We apply the fitted parameters to our newly developed code “Plasma Kinetic Unified Eigenmode Solutions” (PKUES; Luo et al. 2022) and find an unstable mode with an angle between wavevector k and the local mean background magnetic field $\mathbf{B}_{0, \text{local}}$ of $\theta_{k, B_0} = 5^\circ$, which is consistent with our observations (Figure 1(e)). The first part of the PKUES code is inherited from PDRK (Xie & Xiao 2016), which solves the linear Vlasov equation and calculates all eigenmode solutions at a time. Moreover, PKUES incorporates polarization functions of The New Hampshire Dispersion Relation Solver (Verscharen & Chandran 2018), which provides a full set of the characteristic fluctuations of the magnetic field ($\delta\mathbf{B}$), the electric field ($\delta\mathbf{E}$), the velocity ($\delta\mathbf{V}_j$), and the VDF (δf_j). We find only one unstable mode branch (Figure 2(c)). Typically, there are four modes associated with the bi-Maxwellian fitting result (Gary et al. 2016; Klein et al. 2021): parallel- and antiparallel-propagating A/IC modes and FM/W modes. In this study, the only unstable mode is the antiparallel-propagating ($\omega_r/\omega_{c,p} < 0$, where ω_r is the wave frequency and

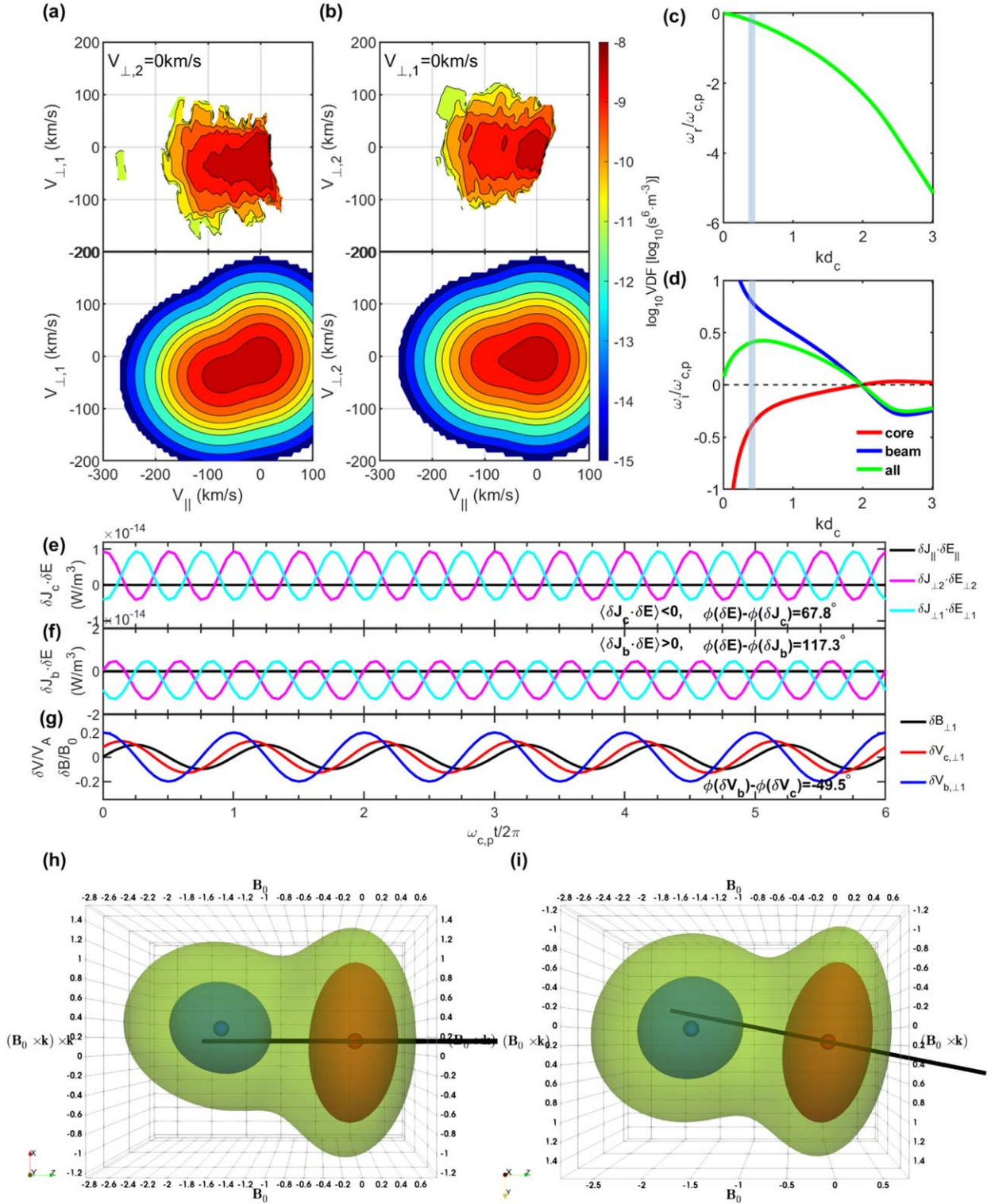


Figure 2. Analysis of the kinetic instability by applying the PKUES code to the observation. (a, b) Slices of the measured VDF at 11:30:18 and the fitted VDF using the GA method. (c) Dispersion relation, $\omega_r/\omega_{c,p} - kd_c$, of the unstable wave branch. (d) The normalized growth rate ($\omega_i/\omega_{c,p}$) contributions from proton core (red line), proton beam (blue line), and the sum of all species including the contribution of electrons (green line). The shaded area indicates $kd_c = 0.41$, the scale at which the frequency corresponds to the observed cyclotron wave frequency in the plasma frame. (e–f) Time series of the energy conversion rates in the three directions (\parallel , $\perp 1$, $\perp 2$). (g) Time series of the velocity fluctuations for core and beam, and the magnetic field fluctuation in the direction perpendicular to the background magnetic field. (h, i) Two snapshots of the isosurfaces of the VDFs (red for core, blue for beam, and green for total) at $\omega_{c,p}t/2\pi = 0$, which are viewed from two orthogonal perspectives, both perpendicular to the background magnetic field. The black line denotes the instant magnetic field direction. The red and blue balls mark the instantaneous center of the core and the beam, respectively. The black line cuts through the center of the core to illustrate the angle between the magnetic field and the drift velocity. An animation of a similar layout as panels (h) and (i), which shows the dynamic variation of the non-field-aligned drift between the core and the beam in 3D velocity space associated with the eigenmode wave, is available in the online Journal. The left, top right, and bottom right panels in the animation correspond to the line-of-sight directions along \mathbf{B}_0 , $\mathbf{B}_0 \times \mathbf{k}$, and $(\mathbf{B}_0 \times \mathbf{k}) \times \mathbf{k}$, respectively.

(An animation of this figure is available.)

$\omega_{c,p}$ is the proton cyclotron frequency) FM/W mode, which has a positive dispersion relation ($\partial^2\omega/\partial k^2 > 0$) and right-hand circular polarizations. By finding the intersection point of the dispersion relation with $\omega_{sc}/\omega_{c,p} = \omega_r/\omega_{c,p} + kd_c \cdot \mathbf{U}_c/V_A$, we find a plasma wave frequency of about 0.07 Hz, and the scale is $kd_c = 0.41$ in the proton core rest frame, where ω_{sc} is the observed wave frequency in the spacecraft frame, k is the wavenumber, and d_c is the proton core inertial length. In light of this, we infer that the observed waves are outward-propagating fast magnetosonic waves.

Considering the effects of the core and the beam separately is meaningful to understanding the physics of wave activity. The contributions of different populations (core and beam) to the wave growth/damping are additive in linear theory (Gary 1993). For an unstable mode, it is of great interest to understand the dominant source of free energy and the effects of other populations on the unstable mode, which we cannot learn from the total growth rate alone.

The growth rates of this mode branch and the polarization properties of the mode at $kd_c = 0.41$ are shown in Figures 2(d)–(i). These results are all taken from linear Vlasov theory and calculated using the PKUES code. Figures 2(e)–(g) show the time series of fluctuating quantities, with the horizontal axis denoting the wave period. We take the solutions of PKUES as the initial phase ($t = 0$) and extend them to six wave periods according to the wave frequency. The normalization is chosen arbitrarily to be $|\delta B_{\perp 1}| = 0.1$. To investigate the different roles of the core and the beam populations for the wave growth, we calculate and compare the growth rates contributed from the proton core and the proton beam separately (Figure 2(d)). Specifically, at $kd_c = 0.41$, the beam boosts the wave growth ($\omega_{i,b}/\omega_{c,p} > 0$), while the core suppresses it ($\omega_{i,c}/\omega_{c,p} < 0$), where $\omega_{i,c}$ and $\omega_{i,b}$ denote the growth rate contributed from proton core and proton beam, respectively. The net effect of the two populations leads to the growth of the wave at this scale ($\omega_i/\omega_{c,p} > 0$). The energy transfer rates ($\delta \mathbf{J}_c \cdot \delta \mathbf{E}$ and $\delta \mathbf{J}_b \cdot \delta \mathbf{E}$) for both populations further support this result (Figures 2(e)–(f)), where $\delta \mathbf{J}$ is the fluctuating current density. On average, the energy transfer rate between the wave and the beam is negative ($\langle \delta \mathbf{J}_b \cdot \delta \mathbf{E} \rangle < 0$), suggesting that the beam’s kinetic energy is transferred into the wave’s electromagnetic energy, where $\langle \cdot \rangle$ denotes the time average. At the same time, however, the wave–core interactions transfer energy from the wave to the core particles ($\langle \delta \mathbf{J}_c \cdot \delta \mathbf{E} \rangle > 0$). The energy transfer direction is fundamentally determined by the azimuthal angle (ϕ) correlation between $\delta \mathbf{J}$ and $\delta \mathbf{E}$. The angle between $\phi(\delta \mathbf{E})$ and $\phi(\delta \mathbf{J}_b)$ is greater than 90° , while the angle between $\phi(\delta \mathbf{E})$ and $\phi(\delta \mathbf{J}_c)$ is less than 90° .

The beam velocity fluctuation has a greater amplitude than the core velocity fluctuation, accompanied by the azimuthal angle difference, $\phi(\delta \mathbf{V}_b) - \phi(\delta \mathbf{V}_c) = -49.5^\circ$ (Figure 2(g)). Figures 2(h)–(i) show the snapshots of the 3D VDF viewed in two orthogonal orientations perpendicular to the background magnetic field at $t = 0$. At this phase of the wave, the angle between \mathbf{V}_d and \mathbf{B} is not zero, which means that the beam is not field aligned. Since \mathbf{V}_c , \mathbf{V}_b , and \mathbf{B} all fluctuate at the same frequency, the relative magnitudes and the phase differences among these fluctuating quantities are fixed. This means that during a wave period the angle between \mathbf{V}_d and \mathbf{B} remains constant (i.e., the non-field-aligned drift of the beam), although the non-field-aligned component of the beam drift averages to zero over an entire wave period.

2.3. Observational Evidence of the Non-field-aligned Beam

Non-field-aligned proton beams are potentially present in the solar wind during time intervals with large-amplitude ion-scale waves owing to their intrinsic transverse polarization. To verify this hypothesis, we fit all 612 measured VDFs during the wave event as shown in Figure 1 and obtain all fit parameters for each population including n_j , \mathbf{U}_j , $v_{th\perp j}$, and $v_{th\parallel j}$. We use the method described in Chapter 15 of Press et al. (2007) to calculate the uncertainties of the fit parameters. We calculate $\chi^2 = \sum_i (f_{i,obs} - f_{i,fit})^2 / \sigma$, where σ is the standard deviation of the measurement error as calculated according to Equation (15.1.7) of Press et al. (2007). We assign the 99% confidence level of each parameter to their respective uncertainties. The confidence level is a function of the number of parameters of interest and $\Delta\chi^2$, which is defined as the deviation from χ^2 by adjusting a certain parameter around its fitted value while fixing other parameters with the fitted values. Here, for calculating the uncertainty of a certain parameter, a 99% confidence level, which corresponds to a $\Delta\chi^2$ value of 6.63 (see the table in Chapter 15.6 of Press et al. 2007), is adopted. Figure 3 shows the time series of the fitted velocities of the core and the beam in the RTN coordinates. We can calculate the drift velocity vectors, $\mathbf{V}_{drift} = \mathbf{U}_b - \mathbf{U}_c$ and therefore θ_B , v_{drift} , at all times (Figure 3). The uncertainties are calculated according to the propagation of uncertainty, indicated by the green shaded area in Figure 3. On average, the uncertainties (Δ) related to the core and the beam velocities are as follows: $\Delta U_{c,R} \sim 5.1 \text{ km s}^{-1}$, $\Delta U_{b,R} \sim 8.4 \text{ km s}^{-1}$, $\Delta U_{c,T} \sim 4.8 \text{ km s}^{-1}$, $\Delta U_{b,T} \sim 6.5 \text{ km s}^{-1}$, $\Delta U_{c,N} \sim 5.0 \text{ km s}^{-1}$, and $\Delta U_{b,N} \sim 6.7 \text{ km s}^{-1}$. We obtain the uncertainties of the drift velocity with the method of propagation of uncertainty, as $\Delta V_{drift,R} \sim 9.8 \text{ km s}^{-1}$, $\Delta V_{drift,T} \sim 8.0 \text{ km s}^{-1}$, and $\Delta V_{drift,N} \sim 8.4 \text{ km s}^{-1}$.

We interpolate the magnetic field data to the time stamps of the PAS measurements. Then, we calculate the angle between the drift velocity vector and the magnetic field vector at the cadence of PAS. Figure 4(a) shows a scatter plot of the normalized drift velocity vectors in field-aligned coordinates. A large cluster of points deviates from the instant magnetic field directions, with more points roughly concentrated around $\theta_{B,V_{drift}} \sim 175^\circ$, where $\theta_{B,V_{drift}}$ is the angle between the instant magnetic field vector and the drift velocity vector. Such deviations can also be seen in the probability distribution function (pdf) of $\theta_{B,V_{drift}}$. A maximum pdf value is reached at about $\theta_{B,V_{drift}} \sim 176.5^\circ$ (Figure 3(b)). This value is consistent with the prediction from linear Vlasov theory using the parameters from Figure 2 with $\delta B/B_0 \sim 0.1$, indicating a small but nonzero angle between the relative drift velocity and the magnetic field direction. We calculate the rms fluctuations in B over 1 s because it takes about 1 s for PAS to complete the sampling of a full 3D proton distribution, although the proton distributions are measured every 4 s (Owen et al. 2020). The average rms fluctuations of the magnetic field for B_R , B_T , and B_N over 1 s are about 0.024, 0.062, and 0.062 nT, respectively. Based on the propagation of uncertainty, the angular uncertainty contributed by magnetic field fluctuations is about $0^\circ.01$, which is negligible since it is much smaller than the angular resolution of the VDF. In principle, we should calculate the 1 s average magnetic field to define the magnetic field direction during the corresponding sampling time interval of the PAS. Because the rms value of the magnetic field within 1 s is very small compared to its average value (less than 2% of the average value), we interpolate the magnetic field data to the time stamp

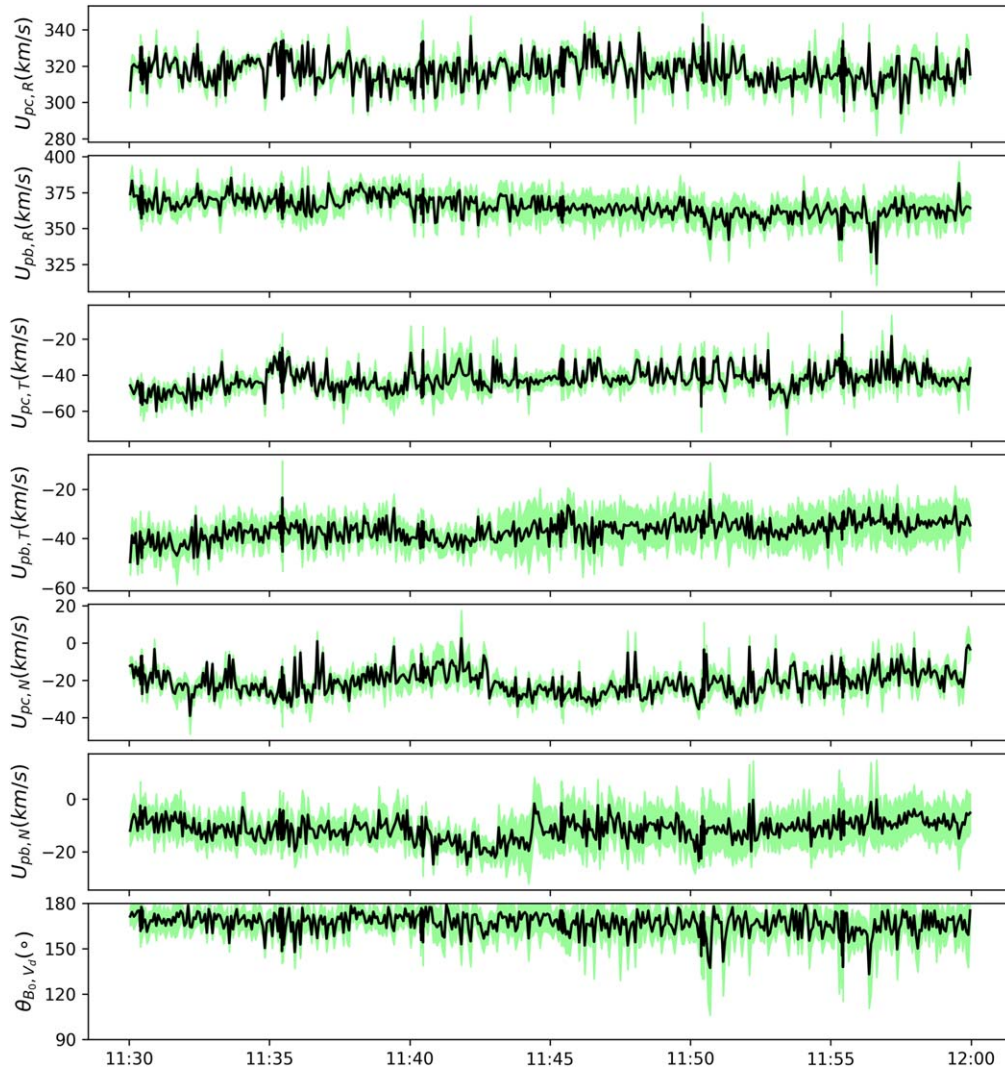


Figure 3. Time series of the core and beam velocities in RTN coordinates, and the angle between the drift velocity vector and the magnetic field direction. The green shaded area denotes the uncertainties of each parameter.

of the PAS data to obtain the magnetic field direction for each measured VDF.

For particle instruments like PAS, the errors due to finite counting statistics propagate into the calculation of the proton bulk properties. We need to take into account the effect of this error in our calculation. First, we obtain the bulk velocity (U_p) and the temperature (T) from plasma moment data that are provided by the PAS team. The bulk kinetic energy (E) is calculated as $E = 0.5m_p U_p^2$, where m_p is the proton mass. The standard deviation of the bulk velocity (σ_{U_p}) is $\sigma_{U_p}/U_p = \sqrt{T/E}/\sqrt{N}$, where N is the total number of counts collected by PAS during its sampling for generating one VDF (Moore et al. 1998; Gershman et al. 2015; Louarn et al. 2021). The standard deviation of the bulk velocity is related to the accuracy in calculating bulk velocity due to the finite number of counts during measurements. The relative contribution to the number of counts from the core (N_c) and the beam (N_b) is proportional to the ratio of the core VDF (f_c) and beam VDF (f_b), i.e., $N_c(\mathbf{v})/N_b(\mathbf{v}) = f_c(\mathbf{v})/f_b(\mathbf{v})$, where $N_c(\mathbf{v}) + N_b(\mathbf{v}) = N(\mathbf{v})$. By summing over all the bins, we then obtain the total counts contributed from the core and the beam. For the core population, on average, $T \sim 10$ eV, $E \sim 540$ eV, and $N \sim 425$,

and we obtain $\sigma_{U_p}/U_p \sim 0.0051$. For the beam population, on average, $T \sim 12$ eV, $E \sim 788$ eV, and $N \sim 1024$, and we obtain $\sigma_{U_p}/U_p \sim 0.0052$. The standard deviation of the direction of the bulk velocity is approximately $\arcsin(\sigma_{U_p}/U_p) \sim 0^\circ 29(0^\circ 30)$. The standard deviation of the angle between drift velocity and background magnetic field is about 2° . The errors due to the quantization effect are discussed in the Appendix. For the magnetic field, the overall absolute error is about 0.1 nT. The contribution of such error to the angular uncertainty is about 1° . Hence, we are confident that the observed non-field-aligned drift velocities do not result from and are less affected by the uncertainties in measurements.

3. Summary and Conclusion

Proton beams are ubiquitous in the solar wind, dynamically affecting the global plasma properties and wave-particle interactions. To investigate the separate roles of the core and the beam in wave growth/damping, we select a wave event lasting about 30 minutes observed by SolO. Based on our observations (Figure 1), we can only conjecture that the observed waves are either outward-propagating FM/W waves or inward-propagating A/IC waves. Using linear Vlasov theory (Figure 2), we find the

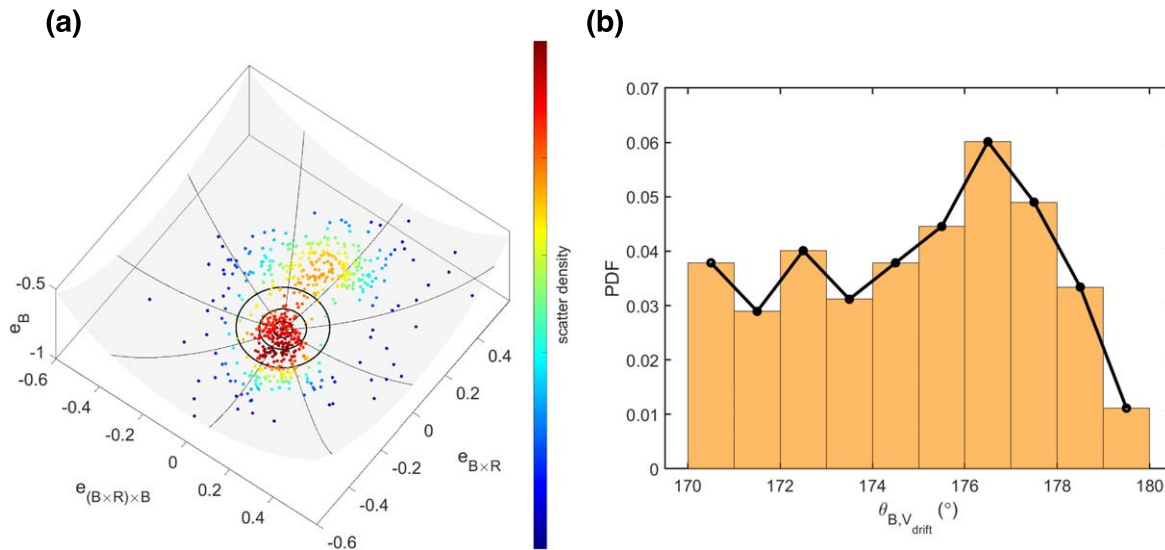


Figure 4. Evidence for the existence of non-field-aligned proton beams during the cyclotron wave activity from the SoLo data set. (a) Scatter plot of the normalized drift velocity vector, in the instant field-aligned coordinates (e_B , $e_{B \times R}$, $e_{(B \times R) \times B}$). The translucent surface is a part of a spherical surface with the radius equal to 1, and all points lie on this surface. The pole is in the direction opposite to the instant magnetic field. The black circles on the surface represent 2° , 5° , and 10° deviations from the anti-field direction. The color of each point stands for the scatter point density around that point, where the red color means that more points are concentrated around that point, while the blue color means fewer points around. (b) The pdf of $\theta_{B, v_{drift}}$ in the range between 170° and 180° .

most likely unstable mode to be the antiparallel-propagating FM/W wave, the properties of which are consistent with our observations. A slower proton core and a faster proton beam are persistently and dynamically present during the wave measurements. Based on linear Vlasov theory, we study the kinetic instability of the observed proton VDF associated with the FM/W waves and thoroughly compare the predictions with observations. The plausible eigenmode solutions show that antiparallel-propagating right-handed waves grow unstable at $kd_{pc} < 2$. Energy is simultaneously transferred from the proton beam particles to the wave fields ($\langle \delta \mathbf{J}_b \cdot \delta \mathbf{E} \rangle < 0$) and from the wave fields to the proton core particles ($\langle \delta \mathbf{J}_c \cdot \delta \mathbf{E} \rangle > 0$). We infer that the beam bolsters the ongoing enhancement of the wave's electromagnetic energy, while the core has the opposite impact, partially suppressing the wave growth.

The traditional view on the differential flow suggests that the beam velocity direction is passively regulated by the core and the magnetic field perturbations, manifesting as drifting parallel to the instant magnetic field direction (Marsch 2012). In this work, we propose that the non-field-aligned beam feature associated with large-amplitude waves is in agreement with the prediction of linear Vlasov theory. The wave-associated velocity fluctuations of the core and the beam are different in both the amplitude and the phase. For the FM/W mode we analyze, the beam velocity fluctuation amplitude is an order of magnitude greater than that of the core. In addition, the core and the beam velocity fluctuations have distinct phase differences relative to the magnetic field fluctuations. For these reasons, the beam's relative drift velocity vector is not aligned with the instantaneous magnetic field throughout a full wave period. This may be a common feature in the solar wind during large-amplitude wave activity.

Statistical investigations of $\theta_{B, v_{drift}}$ during the wave activity interval and comparison with linear Vlasov theory predictions show clear evidence in favor of our perspective on the non-field-aligned proton beam. The wave signatures are pronounced in the spacecraft frame at about 0.2 Hz (5 s). However, the cadence of PAS is 4 s, which means that we can only get at most one VDF within one wave period. Such low cadence leads to a failure in

identifying a clear wave signature in the VDF. Nevertheless, we are still able to observe the instantaneous non-field-aligned signatures since the sampling time for one VDF is 1 s, which is less than the wave period. We note that there is a small difference between the linear theory prediction and our observations. The large-amplitude FM/W waves can cause prominent VDF deformation of each population, as well as the fluctuations of electromagnetic fields. During the 1 s sampling time of PAS, the VDF is fluctuating in response to the FM/W wave. All the wave-associated information in the VDF during this 1 s interval would be recorded in the measured VDF. Hence, the measured VDF is not exactly a snapshot of the VDF at a certain wave phase, but rather an integration result during a phase interval. This effect leads to a broadening of the measured VDF due to the finite-time sampling, appearing as a temperature anisotropy with larger perpendicular temperature (Verscharen & Marsch 2011). In addition, the FM/W waves can very efficiently scatter beam particles, leading to the broadening of the beam population (Verniero et al. 2022). Even though there are no hammerhead distributions as reported in Verniero et al. (2022), the scattering can also play a role in the wave–particle interaction process. These effects raise the uncertainty of our fit parameters.

For future research, the role of the beam in different wave modes and in the turbulent dissipation processes must be explored. A more insightful understanding of the energy transfer channels will take shape by separately considering each part of the particle populations.

Acknowledgments

Solar Orbiter is a space mission of international collaboration between ESA and NASA, operated by ESA. We thank the entire Solar Orbiter team and instrument PIs for data access and support. Solar Orbiter data are available at <http://soar.esac.esa.int/soar/#home>. Solar Orbiter magnetometer operations are funded by the UK Space Agency (grant ST/T001062/1). Solar Orbiter Solar Wind Analyser (SWA) data are derived from scientific sensors that have been designed and created by and are operated under funding provided in numerous contracts from the UK Space

Agency (UKSA), the UK Science and Technology Facilities Council (STFC), the Agenzia Spaziale Italiana (ASI), the Centre National d'Etudes Spatiales (CNES, France), the Centre National de la Recherche Scientifique (CNRS, France), the Czech contribution to the ESA PRODEX program, and NASA. The work at Peking University is supported by the National Key R&D Program of China (2021YFA0718600 and 2022YFF0503800), by NSFC (42241118, 42174194, 42150105, and 42204166), and by CNSA (D050106). D.D. is also supported by China Postdoctoral Science Foundation (2022M720213). D.V. from UCL is supported by the STFC Ernest Rutherford Fellowship ST/P003826/1 and STFC Consolidated Grants ST/S000240/1 and ST/W001004/1. Tim Horbury is supported by STFC grant ST/S000364/1.

Appendix

Elaboration and Assessment of Plasma Parameter Errors Due to Quantization Effect and Measurement Uncertainty

PAS has a finite angular resolution of 5° (Owen et al. 2020), which leads to the quantization of the measured VDF. Measurement uncertainty arises from the specific instrument design and the sensitivity of counting particles. Both of these effects can contribute to the error of the measured VDF.

For the solar wind at a speed of hundreds of kilometers per second (e.g., 500 km s^{-1}), the Alfvénic velocity fluctuations with $\delta U_N \sim 10 \text{ km s}^{-1}$ in RTN coordinates, which are highly correlated with the magnetic field fluctuations, can be well resolved (Wang et al. 2012; Shi et al. 2015). The corresponding angular difference between the bulk velocity vectors of Alfvénic solar wind protons measured at adjacent times is estimated to be about 1° , which is well below the nominal angular resolution of 5° and called sub-bin accuracy. Similarly, the technique of line centroid determination with the subpixel resolution has been widely employed in the optical research of astrophysics (Quine et al. 2007). To assess the influence of the error due to VDF

quantization on the determination of the relative drift between the core and beam components, we devise and carry out a benchmark test that resembles the PAS measurement.

We assume that a PAS-like instrument is measuring a two-component Maxwellian VDF. The background magnetic field is in the x -direction. Here the xyz coordinate is the PAS-like instrument coordinate. The physical parameters of each component are $n_c = 8 \text{ cm}^{-3}$, $n_b = 4 \text{ cm}^{-3}$, $v_{\text{th}\parallel,c} = v_{\text{th}\perp,c} = 40 \text{ km s}^{-1}$, $v_{\text{th}\parallel,b} = v_{\text{th}\perp,b} = 50 \text{ km s}^{-1}$, $U_{x,c} = -300 \text{ km s}^{-1}$, $U_{x,b} = -360 \text{ km s}^{-1}$, $U_{y,c} = U_{z,c} = U_{z,b} = 0 \text{ km s}^{-1}$, and $U_{y,b} = -3 \text{ km s}^{-1}$. In this situation, the angle between the drift velocity and the magnetic field direction is $2^\circ 86'$.

To model the quantization effect, we first calculate the original VDF value that the center of each bin should measure. Then, we convert the VDF value to the number of counted particles with a differential geometric factor $2 \times 10^{-5} \text{ cm}^2 \cdot \text{sr} \cdot \text{eV}/\text{eV}$ (Owen et al. 2020). Then, we calculate the average counts within each bin. We obtain the estimated VDF values influenced by the quantization effect by converting the average number of counts back to the VDF value.

We add an artificial measurement error to the virtually measured VDF. The artificial measurement error is modeled as a normal distribution with the standard deviation being 0.3 of the corresponding VDF value at each bin. The count rate by a particle instrument in principle follows a Poisson distribution, with the parameter in Poisson distribution equal to the expectation of count rate. Mathematically, if the count rate is large enough, the normal distribution, with its mean equal to the count rate expectation and its standard deviation equal to the square root of count rate, is a good approximation to the Poisson distribution. For a count rate greater than 12, 0.3 of the count rate, which is greater than the square root of the count rate, is large enough to serve as a proxy of the measurement error. The original preset VDF, the measured VDF taking into account both errors, and the fitting results are shown in Figure 5. The fitted plasma parameters are shown in Table 1. It

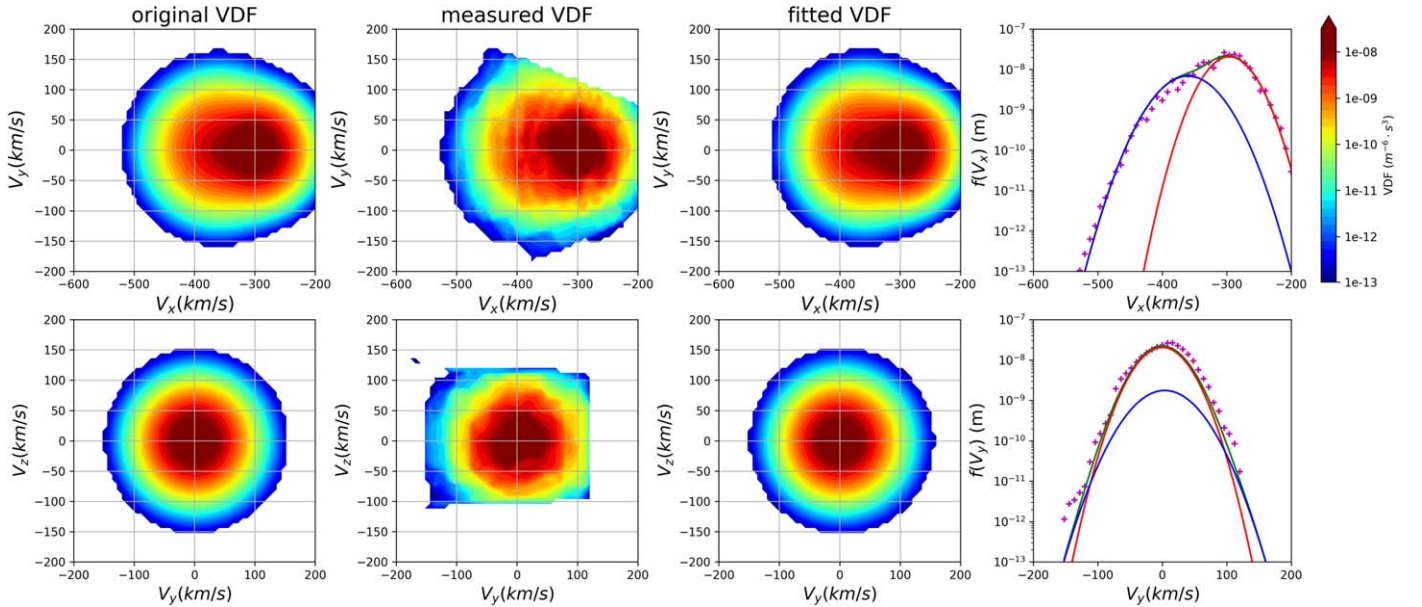


Figure 5. Benchmark test for resolving sub-bin resolution by the fitting process. The left three columns show the results belonging to the presumed VDF (“original VDF”), the measured VDF influenced by quantization effect and measurement error (“measured VDF”), and the fitting results with a two-component bi-Maxwellian distribution. Slices of the VDF at $U_z = 0$ and $U_x = -300 \text{ km s}^{-1}$ are shown in top and bottom panels, respectively. The rightmost column shows the 1D cut of the corresponding VDF (magenta plus sign) and bi-Maxwellian fitted core (red solid line) and beam (blue solid line) through the core center along the x -direction and z -direction.

Table 1
Comparison between the Original VDF and the Fitting Results^a

	$V_{d,x}$ (km s ⁻¹)	$V_{d,y}$ (km s ⁻¹)	$V_{d,z}$ (km s ⁻¹)	θ_{V_d,B_0} (deg)
Original	-60	3	0	2.86
q.fit	-59.86	3.56	0.38	3.42
q+m.fit	-64.73	2.01	0.18	1.79




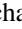


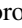
Note.

^a “q.fit” denotes the fitting results of the measured VDF influenced by the quantization effect only, while “q+m, fit” represents the fitting results of the measured VDF influenced by both the quantization effect and measurement error.

can be seen from Table 1 that the fitting process achieves sub-bin accuracy in the drift velocity and its angle relative to the background magnetic field. It can be seen that the fitting results for the VDF influenced by quantization effect largely recover the original VDF.

The angle between the fitted drift velocity and the magnetic field is about 1°79, which is similar to the preset angle of 2°86 and smaller than the width of the angular bin of the electrostatic analyzer. Our test results show that, although the angular resolution of PAS is about 5°, the fitting process has the ability to resolve the plasma parameters with an uncertainty of less than 5° and hence realizes the sub-bin accuracy.

ORCID iDs

Xingyu Zhu  <https://orcid.org/0000-0002-1541-6397>
 Jiansen He  <https://orcid.org/0000-0001-8179-417X>
 Die Duan  <https://orcid.org/0000-0002-6300-6800>
 Daniel Verscharen  <https://orcid.org/0000-0002-0497-1096>
 Christopher J. Owen  <https://orcid.org/0000-0002-5982-4667>
 Andrey Fedorov  <https://orcid.org/0000-0002-9975-0148>
 Timothy S. Horbury  <https://orcid.org/0000-0002-7572-4690>

References

Astudillo, H. F., Livi, S., Marsch, E., & Rosenbauer, H. 1996, *JGR*, **101**, 24423
 Boardsen, S. A., Jian, L. K., Raines, J. L., et al. 2015, *JGRA*, **120**, 10,207
 Bowen, T. A., Bale, S. D., Bonnell, J. W., et al. 2020a, *ApJ*, **899**, 74
 Bowen, T. A., Chandran, B. D. G., Squire, J., et al. 2022, *PhRvL*, **129**, 165101
 Bowen, T. A., Mallet, A., Huang, J., et al. 2020b, *ApJS*, **246**, 66
 Chen, C. H. K., Matteini, L., Schekochihin, A. A., et al. 2016, *ApJ*, **825**, L26
 Cranmer, S. R. 2001, *JGRA*, **106**, 24937
 Cranmer, S. R., Matthaeus, W. H., Breech, B. A., & Kasper, J. C. 2009, *ApJ*, **702**, 1604
 Ďurovcová, T., Šafránková, J., & Němeček, Z. 2019, *SoPh*, **294**, 97
 Farge, M. 1992, *AnRFM*, **24**, 395
 Freeman, J. W. 1988, *GeoRL*, **15**, 88
 Gary, S. P. 1993, *Theory of Space Plasma Microinstabilities* (Cambridge: Cambridge Univ. Press)
 Gary, S. P., Jian, L. K., Broiles, T. W., et al. 2016, *JGRA*, **121**, 30
 Gershman, D. J., Dorelli, J. C. F., Viñas, A., & Pollock, C. J. 2015, *JGRA*, **120**, 6633

He, J., Tu, C., Marsch, E., & Yao, S. 2011, *ApJL*, **745**, L8
 He, J., Wang, L., Tu, C., Marsch, E., & Zong, Q. 2015, *ApJL*, **800**, L31
 He, J., Wang, Y., Zhu, X., et al. 2022, *ApJ*, **933**, 220
 Hellinger, P., Matteini, L., Štverák, Š., Trávníček, P. M., & Marsch, E. 2011, *JGRA*, **116**, A09105
 Hellinger, P., Trávníček, P., Kasper, J. C., & Lazarus, A. J. 2006, *GeoRL*, **33**, L09101
 Hellinger, P., Trávníček, P. M., Štverák, Š., Matteini, L., & Velli, M. 2013, *JGRA*, **118**, 1351
 Holland, J. H. 1992, *SciAm*, **267**, 66
 Horbury, T. S., O’Brien, H., Carrasco Blazquez, I., et al. 2020, *A&A*, **642**, A9
 Huang, J., Kasper, J. C., Vech, D., et al. 2020, *ApJS*, **246**, 70
 Isenberg, P. A., & Vasquez, B. J. 2007, *ApJ*, **668**, 546
 Jeong, S.-Y., Verscharen, D., Wicks, R. T., & Fazakerley, A. N. 2020, *ApJ*, **902**, 128
 Jian, L. K., Russell, C. T., Luhmann, J. G., et al. 2009, *ApJ*, **701**, L105
 Jian, L. K., Wei, H. Y., Russell, C. T., et al. 2014, *ApJ*, **786**, 123
 Kasper, J. C., Klein, K. G., Weber, T., et al. 2017, *ApJ*, **849**, 126
 Kasper, J. C., Maruca, B. A., Stevens, M. L., & Zaslavsky, A. 2013, *PhRvL*, **110**, 091102
 Klein, K. G., Howes, G. G., TenBarge, J. M., & Podesta, J. J. 2014, *ApJ*, **785**, 138
 Klein, K. G., Verniero, J. L., Alterman, B., et al. 2021, *ApJ*, **909**, 7
 Lavraud, B., Kieokaew, R., Fargette, N., et al. 2021, *A&A*, **656**, A37
 Louarn, P., Fedorov, A., Prech, L., et al. 2021, *A&A*, **656**, A36
 Luo, Q., Zhu, X., He, J., et al. 2022, *ApJ*, **928**, 36
 Marsch, E. 1991, in *Physics of the Inner Heliosphere II. Particles, Waves and Turbulence. Series: Physics and Chemistry in Space*, ed. R. Schwenn & E. Marsch (Berlin: Springer), 45
 Marsch, E. 2006, *LRSP*, **3**, 1
 Marsch, E. 2012, *SSRv*, **172**, 23
 Marsch, E., Goertz, C. K., & Richter, K. 1982a, *JGRA*, **87**, 5030
 Marsch, E., Mühlhäuser, K.-H., Schwenn, R., et al. 1982b, *JGRA*, **87**, 52
 Maruca, B. A., Kasper, J. C., & Bale, S. D. 2011, *PhRvL*, **107**, 201101
 Matteini, L., Laker, R., Horbury, T., et al. 2021, *A&A*, **656**, A39
 Matteini, L., Landi, S., Hellinger, P., et al. 2007, *GeoRL*, **34**, L20105
 Moore, T. E., Pollock, C. J., & Young, D. T. 1998, *GMS*, **102**, 105
 Owen, C. J., Bruno, R., Livi, S., et al. 2020, *A&A*, **642**, A16
 Press, W. H., Teukolsky, S. A., Vetterling, W. T., & Flannery, B. P. 2007, *Numerical Recipes: The Art of Scientific Computing* (3rd ed.: Cambridge: Cambridge Univ. Press)
 Quine, B. M., Tarasyuk, V., Mebrahtu, H., & Hornsey, R. 2007, *CoPhC*, **177**, 700
 Santolík, O., Parrot, M., & Lefeuvre, F. 2003, *RaSc*, **38**, 1010
 Servidio, S., Osman, K. T., Valentini, F., et al. 2014, *ApJL*, **781**, L27
 Shi, M. J., XIAO, C. J., LI, Q. S., et al. 2015, *ApJ*, **815**, 122
 Stix, T. H. 1992, *Waves in Plasmas* (New York: Springer)
 Tu, C. Y., & Marsch, E. 1997, *SoPh*, **171**, 363
 Tu, C.-Y., & Marsch, E. 2002, *JGRA*, **107**, 1249
 Tu, C.-Y., Marsch, E., & Qin, Z.-R. 2004, *JGRA*, **109**, A05101
 Verniero, J. L., Chandran, B. D. G., Larson, D. E., et al. 2022, *ApJ*, **924**, 112
 Verniero, J. L., Larson, D. E., Livi, R., et al. 2020, *ApJS*, **248**, 5
 Verscharen, D., & Chandran, B. D. G. 2018, *RNAAS*, **2**, 13
 Verscharen, D., & Marsch, E. 2011, *AnGeo*, **29**, 909
 Wang, X., He, J., Tu, C., et al. 2012, *ApJ*, **746**, 147
 Wicks, R. T., Alexander, R. L., Stevens, M., et al. 2016, *ApJ*, **819**, 6
 Woodham, L. D., Horbury, T. S., Matteini, L., et al. 2021, *A&A*, **650**, L1
 Woodham, L. D., Wicks, R. T., Verscharen, D., et al. 2019, *ApJL*, **884**, L53
 Woolley, T., Matteini, L., Horbury, T. S., et al. 2020, *MNRAS*, **498**, 5524
 Wu, H., Tu, C., Wang, X., He, J., & Yang, L. 2020, *ApJ*, **904**, L8
 Xie, H., & Xiao, Y. 2016, *PIST*, **18**, 97
 Yoon, P. H. 2017, *RvMPP*, **1**, 4
 Zhao, G. Q., Feng, H. Q., Wu, D. J., et al. 2020a, *ApJL*, **889**, L14
 Zhao, G. Q., Feng, H. Q., Wu, D. J., Pi, G., & Huang, J. 2019, *ApJ*, **871**, 175
 Zhao, G. Q., Lin, Y., Wang, X. Y., et al. 2020b, *GeoRL*, **47**, e89720